Nanoscale

PAPER

View Article Online
View Journal | View Issue

Cite this: *Nanoscale*, 2025, **17**, 20989

High-performance all-inorganic CdSe/CdS nanorod-based light emitting diodes enabled by controlled electrophoretic deposition

Nandita Biswas,†[a] Anthony Mullen,†[a] Lin Lyu,†[a] Yongliang Zhang,[a] Charlie O'Mahony,[a] Matthew Snelgrove,[b] Sergey Beloshapkin,[b] Devika Laishram,[a] Jinlei Wu,[a] Syed A. M. Tofail,[a] Christophe Silien,[a] Kevin M. Ryan[c] and Ning Liu *[a]

Electrophoretic deposition can be used to form tightly assembled nanocrystal films at a macroscopic scale, offering tremendous possibilities to exploit the unique functional properties of nanocrystals at a device level. Herein, combining the experimentally measured electrophoretic deposition current time trace with an analytical model, we can estimate the effective single particle charge in solution and obtain information on the morphology and thickness of the film. Using this method, we formed vertically aligned, void-free CdSe/CdS nanorod (NR) films as the emissive layers in red-emitting all-inorganic NR light emitting diodes. To further optimize the performance of these LEDs, Pentaflurothiophenol (PF-BT) molecules were used to passivate the nickel oxide hole transport layer (HTL) surface. With the reduced hole injection barrier into NRs, less leakage current at NiO_x HTL/NR interface and improved NR film morphology, our best performing NR-LEDs achieved a highest external quantum efficiency of 10.8% with a low turn-on voltage of 2.8 V and a maximum brightness (luminance) of 1735 cd m^{-2} at 5.5 V in an all-inorganic LED architecture. Our work provides an effective route for the development of next-generation nanocrystal-based LED displays with facile large-area mass production using cost effective methods.

Received 12th May 2025,
Accepted 16th August 2025

DOI: 10.1039/d5nr01947h

rsc.li/nanoscale

Introduction

Colloidal nanocrystal-based light-emitting diodes (NC-LEDs) have become the next-generation display technology of choice due to their high light-emitting efficiency, adjustable light-emitting wavelength and excellent monochromaticity.[1–3] Significant progress has been achieved in NC-LEDs with organic–inorganic hybrid structures through the use of high quantum yield core–shell quantum dot (QD), whose device external quantum efficiency (EQE) is exceeding 30%.[4,5] However, organic carrier transport layers, such as the widely used poly(3,4-ethylenedioxythiophene):poly(styrene-sulfonic acid) (PEDOT:PSS), are sensitive to ambient condition and humidity, which reduce the stability of LEDs. All-inorganic NC-LEDs have been explored as more stable alternatives.[6,7] Researchers often use metal oxides such as NiO_x, WO_x, and MoO_x as hole-transporting layers in place of organic charge carrier layers to improve device stabilities.[8] The EQE of all-inorganic NC-LEDs has improved rapidly in recent years to reach 10.1%.[9]

In addition to spherical QDs, researchers also explored other types of nanoparticles, such as core–shell semiconductor nanorods (NRs) or quantum-rods (QR) with 1D special morphology as emissive materials in LEDs.[10,11] The properties inherited from core–shell QDs, such as the size-tunable narrow-wavelength emission across visible and near-infrared range and high photoluminescence quantum yield, are still available to core–shell NRs while many unique properties associated with the anisotropy of NRs, for example a faster radiative decay rate, a large Stokes shift and the polarized emission,[12] make NR-based LEDs useful for various applications in the next-generation display technologies. In addition, NRs can minimize the absorption-originated losses compared to QDs and as a result, self-absorption/inter-absorption can be significantly suppressed. This characteristic can lead to an enhanced EQE in the fabrication of colour conversion white LEDs.[13] A table summarizing current state-of-the-art NR-LEDs in both organic–inorganic and all-inorganic architectures is given in Table S1 of the Supplementary Informaton (SI).

Despite these attractive properties, the development of NR-LEDs still faces significant challenges. For example, it is difficult to form a void-free, closely packed colloidal NR film by simple spin-coating or dip coating techniques due to its

[a]*Department of Physics and Bernal Institute, University of Limerick, Castletroy, Co. Limerick, Ireland. E-mail: ning.liu@ul.ie*
[b]*Bernal Institute, University of Limerick, Castletroy, Co. Limerick, Ireland*
[c]*Department of Chemical Sciences and Bernal Institute, University of Limerick, Castletroy, Co. Limerick, Ireland*
†The authors contributed equally to this work.

unique 1D shape. In the past decade, vertical alignment of NRs has been explored as a unique thin-film architecture and great successes have been achieved.[14–17] In current work, a method called electrophoretic deposition (EPD) was utilized to deposit thin NR films. The presence of ligand-induced surface charges on core–shell NRs allows the NRs to be moved by an external electric field in a solution and to eventually be deposited onto the surface of the electrode of opposite polarity to the charge of NRs.[18] Compared to the spin-coating method, EPD leads to denser films and better adhesion of NRs to the substrate due to the larger kinetic energy carried by each nanoparticle during the deposition process. This approach provides a feasible route to form closely packed, crack-free and vertically assembled NRs thin film as the emissive layer in a LED device.[19,20] However, the film morphology and thickness can still vary from one run to another even though great effort had been made to control the concentration of NRs. It is therefore necessary to develop a method to monitor the film growth in real time and obtain information on the thickness and morphology of the films without resorting to advanced microscopy techniques, such as scanning electron and focused ion microscopies, which can be expensive, time consuming and degrade the samples studied.

In current work, we developed an analytical model to describe the deposition current as a function of time, taking into account the charged particle concentration changes caused by the limited volume of the nanoparticle solution. By monitoring the deposition current time trace, we can obtain information regarding the effective single particle charge and clustering in the solution, which showed significant impact on the film morphology. The model also allowed us to predict the thickness of the deposited film from the current time trace. This simple yet effective method allowed us to achieve NR-based all-inorganic LEDs with better control on the crack-free CdSe/CdS core–shell NR film by EPD as the emissive layer.

To further improve the performance of the all-inorganic NR-LEDs, Pentafluorothiophenol (PF-BT) molecules were used to passivate the hole injection layer (NiO_x) surfaces. The incorporation of PF-BT molecules not only promotes the hole injection from HTL to NRs with a favourable electronic band alignment but also effectively passivates the surface trap states of the NiO_x that function as non-radiative recombination centres. From the best performing NR-LEDs, we achieved an EQE of 10.8%, the highest value obtained in all-inorganic NR-LEDs reported so far, with a maximum brightness of 1735 cd m^{-2} and a low turn-on voltage of 2.8 V, showing a great promise for electrically pumped all-inorganic NR-based LEDs in future display applications.

Experimental

Chemicals and materials

All chemicals used in this work were of analytical grade and utilized as received without any further purification. Cadmium oxide (>99%) (CdO), trioctylphosphine (90%) (TOP), trioctylphosphine oxide (99%) (TOPO), selenium (99.98%), sulphur (99%), *n*-tetradecylphosphonic acid (TDPA, 99%), *n*-octadecylphosphonic acid (ODPA), *n*-hexylphosphonic acid (HPA), Pentafluorothiophenol (PF-BT) that was utilized here to passivate the metal surface, zinc acetate dehydrate, ethyl acetate, magnesium acetate and dimethyl sulfoxide, were all purchased from Sigma Aldrich or Fisher Scientific. The substrates *i.e.* silicon (Si) wafers were obtained from University Wafers and ITOs were purchased from Delta Technologies. ZnMgO nanoparticles were purchased from Shenzhen Planck Innovation.

Synthesis of CdSe/CdS core–shell nanorods

CdSe/CdS NRs were synthesized following procedures described in previous reports with some alternation. To synthesized CdSe cores, 79 mg of CdO, 4.5 g of TOPO, 0.335 g of TDPA were added in a 25 mL three-necked flask. The mixture was then heated to 150 °C under argon atmosphere and after reaching that temperature, the mixture was evacuated for one hour in vacuum. Later, when the temperature was raised to 325 °C, the brown color solution changed to clear and colourless, indicating it was ready for the injection of 2.25 mL TOP. Next step was to quickly inject 0.95 mL (1 mol L^{-1}) of Se/TOP stock solution into the flask and kept at this temperature for 10 s. In a typical synthesis of CdSe/CdS nanorods, 0.115 g of CdO, 0.125 g of HPA, 0.6 g of TDPA and 6 g of TOPO were mixed into a 25 mL three-neck flask and the mixture was slowly increased to 150 °C under argon gas. Then, the mixture was degassed for 1 h in vacuum, maintaining the temperature of 150 °C. Eventually, the solution was heated to 300 °C under argon atmosphere to dissolve the CdO until it turned optically clear and colourless. At this point, 3 mL of TOP is quickly injected into the flask. When the temperature reached at 325 °C a mixed solution containing S/TOP (2 mol L^{-1}) and CdSe seeds (0.5 mL) was quickly injected. The reaction was kept at 325 °C for 10 min. After being washed in toluene and IPA mixture, the nanorods are re-dissolved in toluene for further use.

PF-BT passivation of the NiO_x surface

The PF-BT molecules were deposited at the surface of the NiO_x by spin-coating a PF-BT solution (in toluene, 0.01 mg mL^{-1}) at 2500 rpm for 40 s onto ITO/NiO_x substrate. The substrate was then heated to 120 °C for 15 min. The ITO/NiO/PFBT film was then washed in toluene to remove weakly bonded molecules.

Electrophoretic deposition of the CdSe/CdS nanorods layer

The purified CdSe/CdS nanorods were dispersed in anhydrous toluene and then sonicated for 1 h before EPD. The NRs solution was made of various concentrations between 0.5 to 15 mg mL^{-1} (50–1500 mg of CdSe/CdS NRs into 100 mL of anhydrous toluene). The deposition was run at the ambient condition under the external potential of 400 V and the deposition time was set between 180–300 s. The voltage is supplied from a high-voltage power supply unit (TECHNIX SR-5-F-300) and the current was monitored using a digital multimeter. During this EPD process, two electrodes with same size were immersed

into NRs solution keeping a fixed distance of 2 mm apart. After deposition, the electrodes were gently raised from the NRs solution and dried in air for 5 minutes.

Fabrication of all-inorganic LED devices

LEDs were fabricated on ITO glass substrates, which were first cleaned in an ultrasound bath using acetone and isopropanol sequentially for 15 min. Prior to the HTL deposition, the ITO glass was dried with nitrogen (N_2) blowing. The sputtering method was applied to deposit ~35 nm NiO_x hole transporting layer into ITO glass, followed by being annealed at 400 °C for two hours. The sputtering chamber (AJA International) was evacuated to reach less than 1×10^{-6} Pa before the deposition. Commercially available 99.9% pure Ni target was used, and the sputtering was done under 3.6 mTorr pressure with a gas mixture of Ar and O_2. After annealing, the ITO/NiO_x substrate was spin-coated with PF-BT dipole molecules. The CdSe/CdS NR (in toluene, 5 mg mL^{-1}) layer was then deposited by EPD and annealed at 120 °C in air for 15 min to dry up the solvent. Next, ZnMgO nanoparticles (in ethanol, 1 mg mL^{-1}) were spin-coated at 2000 rpm for 3 min and dried at 120 °C in air for 20 min. Finally, Ag as the cathode (~50 nm) was deposited employing thermal evaporator through a shadow mask under a high vacuum of $\sim 1 \times 10^{-7}$ Torr.

Characterizations

The transmission electron microscopy images of the as-synthesized NRs were characterized using a JEOL JEM-2100F transmission electron microscope (TEM) with 200 keV electron beam energy. CdSe–CdS nanorods were drop casted from the diluted solution onto a 100-mesh carbon-coated copper grid. GI-XRD of the thin films was performed in parallel-beam geometry on an Anton Paar XRDynamic 500 diffractometer (Cu Kα, λ = 1.5406 Å, 40 kV, 50 mA) with a goniometer radius of 360 mm. A scan speed of 9 s per step and a step size of 0.02° in 2θ was used. The angle of incidence (ω) was fixed at 1° whilst the detector was moved along the 2θ circle. The optics included a fixed divergence slit of 0.065°, in addition to a 0.05 rad Soller slit and 0.005 parallel plate collimator on the incident and diffracted beam path respectively. This setup maximises the signal arising from the thin film with respect to the substrate, by limiting X-ray penetration into the sample.

KPFM was performed using an Ntegra Spectra scanning probe microscope (SPM) operated in Frequency Modulation (FM-KPFM). An AC voltage of 0.69 V RMS was applied between the conductive probes, along with a 5 V DC bias and the grounded samples at a frequency of 112.5 kHz. The cantilever used for this measurement was a HA_NC – Pt tip.

The PL spectrum of the NRs solution was collected by an Ocean Optics HR4000+ spectrometer under an excitation wavelength of 405 nm. Here, the excitation power and collection filter were 2.0 mW and 450 nm long pass filter respectively. The absolute photoluminescence quantum yield of the NR film was measured by using an integrating sphere coupled with an Ocean Optics Flame spectrometer. The current–voltage and luminescence-voltage characteristics were measured using a Keithley 2602B source, Thorlabs 4P3 integrating sphere, and an HMO3004 oscilloscope coupled to a calibrated PDA200C photodiode amplifier from Thorlabs. The EQE was calculated as the ratio of the photon flux and driving current of the device. The electroluminescence (EL) spectra of the devices were obtained by using an Ocean Optics HR4000+ spectrometer.

Results and discussion

Rate equations for electric field assisted nanoparticle deposition from non-polar solution

The basic working principles of EPD can be found in many textbooks on colloidal particles.[21,22] Some excellent work on applying EPD method for structured nanomaterials and discussions of its mechanisms can be found in ref. 23 and 24. Our model considers the concentration changes caused by the finite volume of the nanoparticle (NP) solution, which is around 6 ml in most of our experiments, and the dissolution of the NPs back to its solution. More details of the model are discussed in the SI. To summarize, if only one type of NPs is considered in the solution, the coupled equations below can be used to describe the deposited mass and concentration change of NP solution with time:

$$\begin{cases} \dfrac{dw}{dt} = R_{dep} - R_{dis} & (1) \\ R_{dep} = Im/q & (2) \\ I = \dfrac{c_c v A q}{m} & (3) \\ c_c = c_0 - \dfrac{\int R_{dep} dt}{V} & (4) \end{cases}$$

where w is the deposited mass on the substrate, R_{dep} the deposition rate, R_{dis} the dissolution rate, I the deposition current, c_c the concentration of charged particles in solution, A the deposition area of the electrode, v the velocity of the NPs, q the charge of the single NP, m the mass of single particle, V the volume of the solution and c_0 the initial concentration of charged particles. As discussed in ref. 23, the velocity of NPs under a constant electric field reaches a steady state of $qE/(6\pi r\eta)$ in less than a couple of nanoseconds. Here r indicates the radius of a spherical particle and η is the viscosity of the solution.[25] The electric field E is considered as a constant in our model. The validity of this assumption will be discussed further in next section. In our EPD time scale of tens to hundreds of seconds, the NP velocity can be approximated by the steady state constant. With this approximation, the current (I) is directly proportional to the charged particle concentration c_c *via* eqn (3). If we represent R_{dep} and c_c using current I and plug them into eqn (4), we then get a differential equation of I as:

$$\frac{dI}{dt} = -\frac{qEA}{6\pi r\eta V} I \quad (5)$$

Its solution is an exponential decay function $I = I_0 e^{-\frac{t}{\tau}}$, with the time constant $\tau = \dfrac{6\pi r\eta V}{qEA}$, and $I_0 = c_0 \dfrac{qV}{\tau m}$. This means that from the experimentally measured decay constant τ and initial

current I_0, we can obtain the single particle charge q once all other values are known. This single exponential decay behaviour is true for monodispersed NPs. If other species or clustering of NPs exist in the same solution, the sum of multiple exponential decay curves is expected. The mass deposition rate R_{dep} can then be calculated from the measured current I *via* eqn (2).

Once the dissolution rate R_{dis} is known, we can also estimate the net mass deposition on the substrate *via* eqn (1). As discussed in the SI, our experimentally measured dissolution rate R_{dis} is proportional to the NP mass left on the substrate. Eqn (1) can then be re-written as:

$$\frac{dw}{dt} = \frac{I_0 m}{q} e^{-\frac{t}{\tau}} - \gamma w \quad (6)$$

The solution to eqn (6) is:

$$w = w_0 \left(e^{-\frac{t}{\tau}} - e^{-\frac{t}{\tau_{dis}}} \right) \quad (7)$$

where $w_0 = \frac{I_0 m}{q} \frac{\tau\tau_{dis}}{\tau - \tau_{dis}}$ and $\tau_{dis} = \frac{1}{\gamma}$. Since τ_{dis} can be measured experimentally, we can obtain the w as a function of time. From eqn (7), we can also calculate the time for the deposited mass reaching its maximum value $t_{max} = \frac{\tau\tau_{dis}}{\tau - \tau_{dis}} (\ln\tau - \ln\tau_{dis})$ with a maximum mass deposition of $w_{max} = \frac{I_0 m}{q} \frac{\tau\tau_{dis}}{\tau - \tau_{dis}} \left(e^{-\frac{t_{max}}{\tau}} - e^{-\frac{t_{max}}{\tau_{dis}}} \right)$.

CdSe/CdS NR deposition by EPD

In this work, the CdSe/CdS core–shell NRs were synthesized *via* a seeded-growth method detailed in the Experimental section, which was slightly modified from that reported by Carbone *et al.*[26] The core size of the NRs could be controlled by alternating the reaction time, temperature and types of phosphonic acid ODPA or TDPA.[27] The aspect ratio of the synthesized CdSe/CdS NRs can also be changed between 2.5–7. One batch of NRs with an aspect ratio of 5.5 was confirmed by the TEM images (Fig. S4) whereas the mean length and width of the NRs were 33 ± 2 nm and 6 ± 0.5 nm respectively. The optical properties of the CdSe core and CdSe/CdS core–shell NRs are also shown in Fig. S4. The CdSe/CdS NRs maintain high photoluminescence (PL) intensity and high PLQY in both solution and in films (35%–40%). The CdSe core and CdSe/CdS NR exhibit the emission peak centred at 530 nm and 612 nm respectively with a full width at half maximum (FWHM) of 26 nm and 20 nm respectively, consistent with the literature.[28]

These colloidal CdSe/CdS NRs are stabilized in solution by repulsive electrostatic interactions. The surface charge on NRs strongly influences the assembly of these nanocrystals onto films and super-lattice structures.[29,30] In our experiments, two pieces of electrodes, PF-BT treated NiO_x/ITO sample and ITO with the same dimensions, were used as the two conductive electrodes in the EPD set-up. It is essential to keep the two electrodes in parallel positions to establish a uniform electric field for EPD. The NRs were deposited on both electrodes, even though more mass was observed on the negative electrode, suggesting more positively charged NRs in the solution. Meanwhile, the NRs possessing a permanent dipole moment[31] feel a torque which rotates them and causes alignment of the long axis of the NRs with the direction of the electric field.

Fig. 1(a) shows deposition current *vs.* time curves from three EPD depositions, named EPD1 to EPD3 in the following texts. The NR concentration for EPD1 and EPD2 are both 15 mg ml^{-1}. However, their profiles are significantly different. EPD1 curve can be fitted by a single exponential decay function with a fitted time constant τ_{fit} = 1226 ± 13 s. The fitted result agrees well with the predicted time constant from eqn (5) $\tau_{predict}$ = 1341 s (parameters discussed in SI), with the 8.6% difference likely stemming from the NR concentration uncertainty and/or the effective radius r of the NRs. This single exponential decay behaviour suggests that the solution for EPD1 contains one type of well dispersed NRs. The fitting to EPD1 yields an effective single particle charge of 0.3 ± 0.02 e, consistent with the ones reported in the literature.[29] On the other hand, EPD2 curve can only be fitted by a sum of two exponential decay functions with τ_1 remaining 1226 s and τ_2 = 34 ± 0.4 s. This can be explained by either other species in the solution or clustering of NRs. The clusters carry much larger charges, therefore contribute significantly to the initial fast decay of the current, but only account for 1.2% of the total mass of the NPs in the solution according to our fitting. Fig. 1(b) and (c) show the scanning electron microscopy (SEM) images of top surface of CdSe/CdS NRs films after EPD1 and EPD2, respectively. We can see that the surface formed by EPD1, with one type of well disperse NRs, is more uniform than that formed by EPD2, with at least two types of species with two different decay constants. With this understanding in mind, we can speculate the film uniformity from the deposition current time trace directly. The solution for EPD3 has NR concentration of 5 mg ml^{-1},

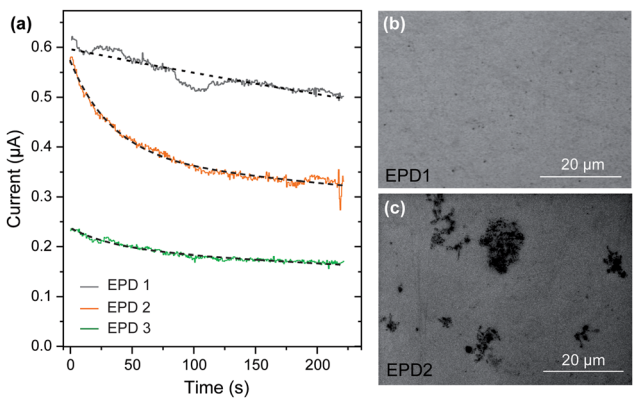

Fig. 1 (a) EPD deposition current *vs.* time traces from three samples. The dashed curves are fitted curves. EPD1 is fitted with a single exponential decay function while EPD2 and EPD3 are fitted with the sum of two exponential decay curves. (b and c) SEM images showing the surface morphology of NR films after EPD1 and EPD2.

yielding the initial current about 1/3 of that for EPD1, consistent with our model.

As discussed in ref. 24, the electric field distribution in the solution can change from the initial value due to the deposition of the NPs on the surface. In our experimental setup, 350–400 V was applied between the two electrodes, the deposited NR film can support current four orders of magnitude larger than that shown in Fig. 1(a) under 7 V (as shown in later figures). We expect the potential drop across the NR film is less than 5% of total potential across the solution, therefore our initial assumption of constant E field is reasonable in our experiment (see SI for more information).

For our experiments, the smoothest films were obtained when these CdSe/CdS NRs were washed two/three times before being used in EPD. Washing more than three times may produce clumpy films that are attributed to the partial loss of capping ligands in washing cycles. An electric field strength of 200 V mm^{-1} was used to obtain vertically alignment of NRs on the conductive substrate. As shown in Fig. S5, weaker electric field strength leads to films with NRs mostly aligned horizontally on the substrate. This alignment is also sensitively dependent on the capping ligands on the NRs and the aspect ratio of the NRs. The thickness of the NRs layer can be controlled by the deposition time, voltage and concentration of NRs suspension, as discussed above. Being accelerated in the DC electric field, the NRs arriving at the conductive substrate with significant kinetic energy, ensures that the NR film formed by EPD maintaining strong contact with the substrate surface and between themselves.

CdSe/CdS NR film by EPD as the emissive layer in an all-inorganic LED

The understanding developed in previous sections allowed us to control better the morphology and thickness of the EPD films. These films were used in a multi-layered architecture for all-inorganic NR-LEDs with ITO (anode)/NiO_x (HTL)/CdSe–CdS (EML)/ZnMgO (ETL)/Ag (cathode), where the CdSe/CdS core–shell NR films as the emissive layer, is illustrated in the diagram of Fig. 2(a). A SEM image of the cross section of a typical device is given in Fig. 2(b). Fig. 2(c) illustrates the energy band diagrams of the NR-LEDs. (See Fig. S6 for the determination of CdSe/CdS conduction and valence band positions.) In this case, holes and electrons are injected into NRs layer *via* NiO_x HTL and ZnMgO electron transport layer (ETL), respectively, under forward bias. As an alternative to the organic hole injection layer, the popular inorganic HTL, NiO had been used widely in all-inorganic NC-LED fabrications.[32–34] In our experiments, NiO was used as both hole injection and hole transport layer. The use of thermally robust NiO has shown higher stability under the high current injection and at the ambient condition. Nevertheless, it is difficult to control the nonstoichiometric charges across a NiO_x surface formed by reactive sputtering of Ni in O_2, which serve as localized electron trapping centres. The XPS spectra of NiO_x film that we grew are given in Fig. S7 and their analyses are summarized in Table S2 of SI. In addition, the energy

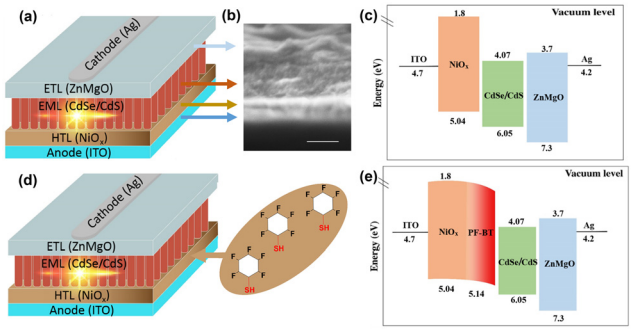

Fig. 2 Device architecture and band diagram of all-inorganic NR-LED employing PF-BT molecular dipoles. Schematic illustrations of NR-LED (ITO-anode/NiO_x-HTL/CdSe–CdS-EML/ZnMgO-ETL/Ag-cathode) and energy level diagram of (a and c) with bare NiO_x HIL and (d and e) with PF-BT molecules between HTL and EML interface respectively. Panel (b) shows an SEM image of the cross section of a typical NR-LED with a configuration given in panel (a). The scale bar indicates 100 nm.

barrier between NiO_x HIL and NC layer leads to excess holes accumulated at the NiO_x surface, affecting the device performance negatively *via* the luminance quenching. To overcome these challenges, we used small polar molecules at the interface of NiO_x/NRs to passivate NiO_x defects.[35] In particular, we followed the recipe demonstrated by Rhee and *et al.*[36] by incorporating a single layer of PF-BT molecules on the NiO_x surface, which had shown to improve the hole injection properties of the QD-LED devices because of their polar nature. The PF-BT molecular dipoles tend to shift the position of the work-function of HIL based on the terminating group present in its backbone,[36] therefore reduce the energy barrier between the HIL and the emissive layer effectively, improving the performance of all-inorganic LED devices. In our experiments, a layer of PF-BT molecules was spin-coated on NiO_x HTL (PF-BT@NiO_x) (Fig. 2(d)). PF-BT@NiO_x film was then undergone annealing at 120 °C and followed by a washing step in toluene to eliminate the excessive molecules that are weakly bounded to the surface. The energy alignment across the multilayer is then modified, where the valence band energy levels of the NiO_x HTL is downshifted to facilitate the injection of the holes into the NR layer, as shown in Fig. 2(e). In this structure, ZnMgO nanoparticle film was chosen as ETL due to its high electron mobility and matched conduction band level with that of NRs emissive layer.[37] The valence band edges of NiO_x and PF-BT@NiO_x were obtained experimentally as discussed in the following section.

Characterizations of PF-BT treated NiO_x HTL

The effect of PF-BT on NiO_x was first investigated using SEM, as shown in Fig. 3(a and b). The surface morphology of the NiO_x film (NiO_x/ITO) formed by the reactive sputtering of Ni in O_2 followed by annealing the sample at 400 °C is significantly different from that of the PF-BT passivated NiO_x film (PF-BT@NiO_x/ITO). The white patchy features on the SEM image of NiO_x suggest regions with surface trapping centres, where elec-

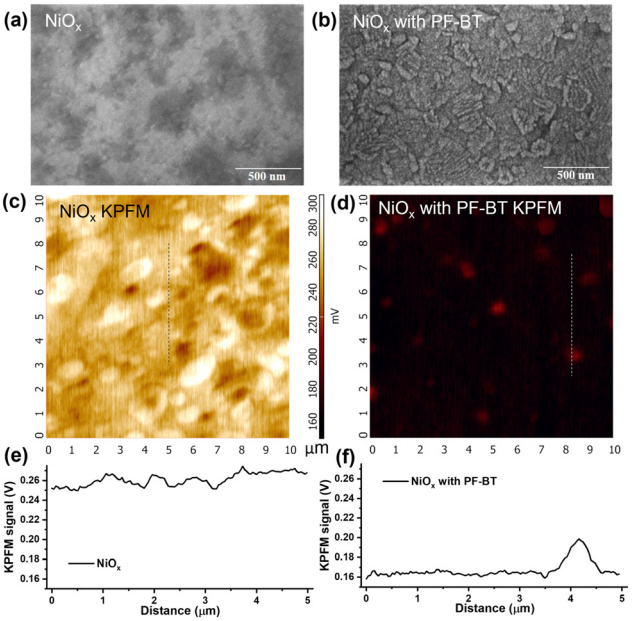

Fig. 3 SEM images of (a) NiO_x film on ITO and (b) PF-BT molecules passivated NiO_x/ITO, (c and d) Kevin Probe Force Microscopy (KPFM) images for NiO_x/ITO film before and after surface treatment with PF-BT molecules, respectively. (e and f) Line profiles of KPFM signal along the dashed lines indicated in (c) and (d).

trons are accumulated and charging effect takes place during the SEM scanning. On the contrary, once PF-BT molecules are deposited onto the NiO_x film, well defined domains of NiO_x can be clearly observed, consistent with what was reported in the literature,[38] suggesting that the surface trapping centres in the original NiO_x film are well passivated. Please note that the PF-BT monolayer is not visible in the SEM images.

To confirm the surface potential difference of the NiO_x films before and after PF-BT molecules passivation, Kevin probe force microscopy (KPFM) images were obtained on both surfaces as shown in Fig. 3(c) and (d). Both images are plotted against the same colour palette, so the surface potential difference is clearly visible from the colour difference. After calibrating against Au and Al substrates with work functions 5.1 eV and 4.3 eV respectively[39] (Fig. S8) using the same Pt coated tip (work function 5.3 eV), we can estimate the work function of NiO_x films/ITO substrate as 5.04 ± 0.04 eV and that of NiO_x films/ITO substrate after PF-BT passivation as 5.14 ± 0.02 eV. This result is consistent with other literature and suggests that the PF-BT surface passivation lowers the hole injection barrier from PF-BT to the active NRs, potentially improving the injection current of the final devices.

The presence of PF-BT self-assembled monolayer (SAM) is further confirmed by our X-ray photoelectron spectroscopy (XPS). The full survey scans of NiO_x/ITO and PFBT@ NiO_x/ITO samples are given in Fig. S9. Even though there are no significant changes in the Ni $2p_{3/2}$ and O 1s peaks in both films, implying that the crystal structure of NiO_x is retained with or without PF-BT SAM, the S 2p and F 1s binding energies at 144.3 eV and 688.2 eV, attributed to sulphur and fluorine core levels, respectively, are only observed in the PFBT@NiO_x/ITO sample (Fig. 4(a) and (b)). The binding energy of the hydrocarbon peak of C 1s at 284.8 eV was used as the reference (charge correction) for all binding energy calculations. The crystallinity of both films was further characterised by grazing-incidence X-ray diffraction (GI-XRD), and the results are presented in Fig. 4(c). The 2θ peaks at 37.1°, 43.1°, 62.5°, 75.3° and 78.9° match the positions for the cubic NiO (111), (200), (220), (311) and (222) planes, as indicated by the black lines in the figure (ICDD 00-047-1049). The other peaks are associated with ITO. The same XRD peaks observed for both NiO_x/ITO and PFBT@ NiO_x/ITO samples suggest that the PFBT passivation did not alter significantly the crystal structures of the underlying NiO_x layer.

To evaluate the hole transport properties of PF-BT modification to NiO_x HTL, two types of hole-only devices (HOD) were fabricated following a configuration depicted in the inset of Fig. 4(d), with the thickness of each layer as ITO (35 nm)/NiO_x (30 nm)/NRs (~60 nm)/NiO_x (50 nm)/Ag (50 nm). The only difference between the two HODs is the PF-BT layer. Compared to the reference device (without PF-BT layer), the presence of the PF-BT dipole layer enhances the current for voltages above 2 V, attributed to the reduction of the energy offset between the NiO_x and NRs by the dipole layer. In addition, the presence of the molecular interlayer reduces the leakage current from NRs to NiO_x below 1 V significantly from 13.5 mA cm^{-2} to 1 mA cm^{-2} due to the passivation of NiO_x surface states. The current density of HOD with PF-BT is also

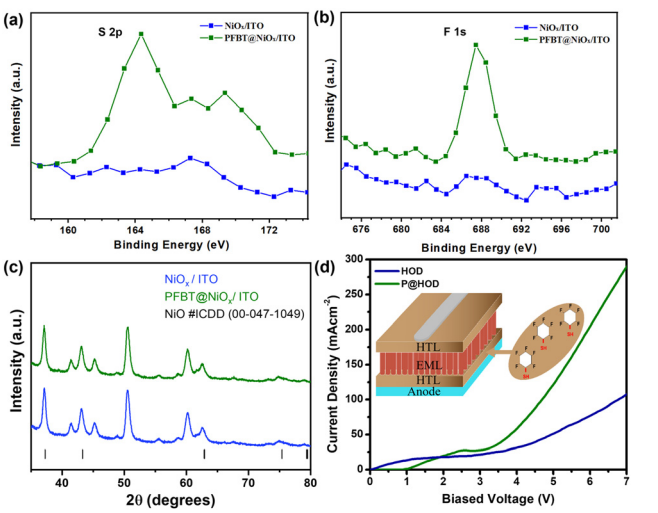

Fig. 4 (a and b) XPS spectra of S 2p and F 1s states for PFBT@ NiO_x/ITO sample, respectively. The XPS spectra on NiO_x/ITO at the same binding energy range are given as the reference. (c) GI-XRD patterns of PFBT@ NiO_x/ITO and NiO_x/ITO. The black bars are used to indicate the corresponding NiO peaks in reference to ICDD 00-047-1049. (d) Schematic drawing of PF-BT Passivated hole-only device where the device structure is ITO/PF-BT@NiO_x/CdSe/CdS/NiO_x/Ag and current density (J)–voltage (V) characteristics of Hole only devices without *versus* with PF-BT passivated NiO_x HTLs (P@HOD).

more comparable with that of the electron only device (Fig. S10), suggesting a more balanced charge injection for later LED devices.

Device performance

The above approaches to optimize the energy levels of the HTL and the morphology of the active NR layer are orchestrated to realize high performance all-inorganic NR-LEDs. NR-LEDs are fabricated in a multi-layered structure of ITO (35 nm)/NiO_x (35 nm)/PF-BT (<1 nm)/NRs (~60 nm)/ZnMgO (25 nm)/Ag (50 nm), where NiO_x HTL is modified by molecular dipoles as discussed above. Fig. 5(a) shows a SEM cross section image of a typical device, where vertically aligned two layers of NRs are clearly observed. Fig. 5(b) shows a photograph of one of the best performing devices operating at 3.5 V, showing uniform red-light emission across the whole electrode (~3 mm^2). The characteristics of the NR-LED (P@LED) are given in Fig. 5(c)–(f). As a comparison, some of the parameters of a non-passivated NR-LED are given in Table 1. In the P@LED case, the *J–V* curve exhibits typical diode-like behaviour, indicating the successful fabrication of the device. When the applied voltage exceeds the turn-on voltage, the current starts to increase rapidly, and the emitting light can be detected. The turn-on voltage of non-passivated LED device is 3.0 V. The P@LED exhibits a slightly lower turn-on voltage of 2.8 V, indicating an efficient injection of holes into the NR-LED. We also found that the current density of passivated LEDs is substantially higher than those of the NR-LEDs without passivation in the bias range of 1–7 V, for instance, 6.1 and 10.0 mA cm^{-2} at 4 V from the non-passivated LED and P@LED device respectively, which gives nearly a 2-fold increase in forward current. The reason behind the higher injection current lies in the reduced valence band offset between the NiO_x and NRs, consistent with the literature.[36]

Table 1 Summary of the device performance of all-inorganic NR-LEDs without dipole layer and with PF-BT on NiO_x

Device	Peak EQE (%)	Turn-on voltage (V)	Peak luminance (cd m^{-2})
LED	0.8	3	228
P@LED	10.8	2.8	1735

The passivation of surface states at the NiO_x surface substantially decreases the non-radiative leakage current and the reduced valence band offset between the NiO_x and NRs leads to higher and more balanced carrier injection into the emissive NR layer. Both factors contribute significantly to the overall performance enhancement to the P@LED. In addition to the increase of current density, the luminance increases as well. Fig. 5(d) shows that the device brightness reaches a maximum of 1735 cd m^{-2} (at 5.5 V) for the P@LED, more than 7-times increases compared to the device without passivation (228 cd m^{-2} at 6.6 V). As the current density and luminance both increase after the incorporation of PF-BT, the EQE is also observed to increase significantly as shown in Fig. 5(e). The peak EQE reaches at 10.8% at 3.8 V, compared to the 0.8% @4.4 V of EQE obtained for the non-passivated LED device.

We did notice the EQE droop in our devices, which can be attributed to multiple factors, such as charge injection imbalance, Auger recombination, and Joule heating.[40] From Fig. 5(e), we can see the efficiency roll-off is highly nonlinear *vs.* applied voltage (current). Auger recombination, which is a nonlinear nonradiative recombination process and contributes significantly to the EQE droop of CdSe/CdS QD-based LEDs,[41] is speculated as one of main reasons for this efficiency roll-off. After 6.5 V, the luminance drops rapidly while the current still increases linearly. In this range, Joule heating could be another source of the EQE droop, which has been observed on NC-based LEDs fabricated on glass substrates.[40] More investigations will be carried out to pin-point the actual cause (s) of the EQE droop at high voltage range for our devices in the future.

The EL spectrum of the P@LED is displayed in Fig. 5(f). The symmetric and narrow EL emission peak of P@LED is centred at 615 nm @ 5 V with full width half-maxima (FWHM) of 30 nm. It is highlighted that the EL spectrum for P@LED shows no parasitic emission, which suggests that the device excitons are effectively generated and recombined inside the NRs emitting layers.

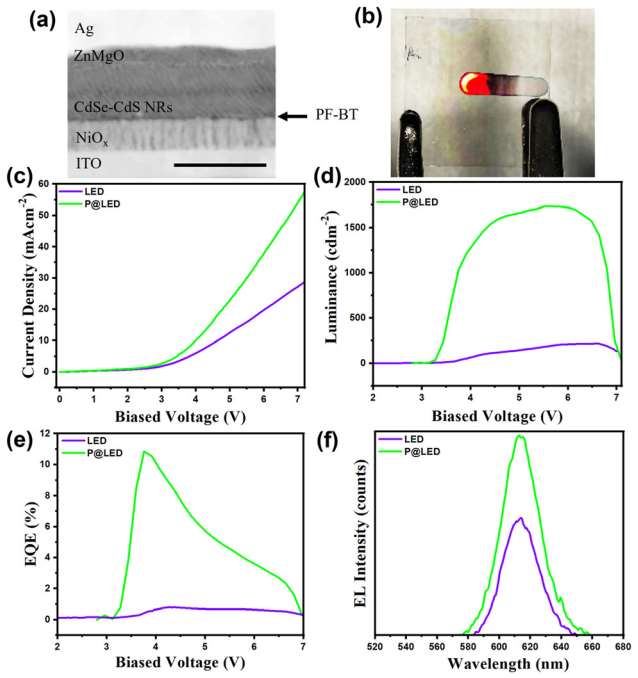

Fig. 5 Comparison of the NR-LEDs device performances with and without PF-BT. (a) Transmission electron microscopy image of the cross section of a typical P@LED device. The scale bar indicates 100 nm. (b) A photograph of a P@LED device operating at 3.5 V. (c) Current density *vs.* biased voltage characteristics, (d) luminance *vs.* biased voltage characteristics, (e) external quantum efficiency (EQE) *vs.* biased voltage, and (f) electroluminescence of two best performing NR-LED devices with and without PF-BT.

Conclusions

In summary, we established an analytical model to describe the EPD process of NPs from a non-polar solution, which was used to obtain information on the morphology, thickness of the deposited film and the effective single particle charge of NPs in solution. With the better control on the formation of vertically aligned CdSe/CdS NR film as an emissive layer and the metal oxide HTL surface modified by PF-BT molecular dipoles, the performance of all-inorganic NR-LEDs are greatly enhanced. Such a passivation process with dipole molecules tunes the energy levels of the HTL, leading to more efficient charge carrier injection and suppression of the trap-medicated non-radiative recombination. As a result, an enhanced luminance is obtained from 228 cd m^{-2} for non-passivated device to 1735 cd m^{-2} for device passivated with PF-BT. The passivated all-inorganic CdSe–CdS NR-based LED devices deliver a high EQE of 10.8%. We anticipate that this metal oxide surface passivation procedure incorporated with NRs alignment provides a fruitful way to realize all-inorganic NR-LEDs with high brightness and low turn-on voltage. Furthermore, this vertical alignment features improved charge transport along the long axes of the NRs[19] and in film emission, which could be of particular importance for the future development of electrically pumped NR-based lasers.

Conflicts of interest

There are no conflicts to declare.

Note added after publication

This article replaces the version published on 26 August 2025, which contained an error in the Results and discussion.

Data availability

The data supporting this article have been included as part of the SI. More information on the modelling of the EPD current time trace and the characterisations of the NRs and the samples can be found in the SI. See DOI: https://doi.org/10.1039/d5nr01947h.

Acknowledgements

This publication has emanated from research conducted with the financial support of Taighde Éireann – Research Ireland, under Grant numbers 17/CDA/4733, 12/RC/2276_P2, 18/EPSRC-CDT/3585, IRCLA/2017/285 and the Engineering and Physical Sciences Research Council EP/S023321/1. This work also received funding from the European Union's Horizon 2020 research and innovation programme under the Marie Skłodowska-Curie grant agreement No. 801165, as well as supports from the National Natural Science Foundation of China (Grant No. 12204088) and joint project of the Science and Technology Programme of Liaoning Province (2023JH2/101700016).

References

1 X. Y. Li, Y. B. Zhao, F. J. Fan, L. Levina, M. Liu, R. Quintero-Bermudez, X. W. Gong, L. N. Quan, Z. Y. Y. J. Fan, S. Hoogland, O. Voznyy and Z. H. Lu, *Nat. Photonics*, 2018, **12**, 159–164.
2 W. R. Cao, C. Y. Xiang, Y. X. Yang, Q. Chen, L. W. Chen, X. L. Yan and L. Qian, *Nat. Commun.*, 2018, **9**, 2608.
3 S. K. Gupta, M. F. Prodanov, W. L. Zhang, V. V. Vashchenko, T. Dudka, A. L. Rogach and A. K. Srivastava, *Nanoscale*, 2019, **11**, 20837–20846.
4 J. J. Song, O. Y. Wang, H. B. Shen, Q. L. Lin, Z. H. Li, L. Wang, X. T. Zhang and L. S. Li, *Adv. Funct. Mater.*, 2019, **29**, 1808377.
5 H. B. Shen, Q. Gao, Y. B. Zhang, Y. Lin, Q. L. Lin, Z. H. Li, L. Chen, Z. P. Zeng, X. G. Li, Y. Jia, S. J. Wang, Z. L. Du, L. S. Li and Z. Y. Zhang, *Nat. Photonics*, 2019, **13**, 192–197.
6 F. Cao, Q. Q. Wu, Y. Z. Sui, S. Wang, Y. J. Dou, W. H. Hua, L. M. Kong, L. Wang, J. H. Zhang, T. Jiang and X. Y. Yang, *Small*, 2021, **17**, 2100030.
7 F. Z. Wang, Z. Y. Wang, X. D. Zhu, Y. M. Bai, Y. Yang, S. Q. Hu, Y. Q. Liu, B. G. You, J. Wang, Y. Li and Z. A. Tan, *Small*, 2021, **17**, 2007363.
8 Q. L. Xu, X. Y. Li, Q. L. Lin, H. B. Shen, H. Z. Wang and Z. L. Du, *Front. Chem.*, 2020, **8**, 265.
9 F. Wang, Z. Wang, X. Zhu, Y. Bai, Y. Yang, S. Hu, Y. Liu, B. You, J. Wang, Y. Li and Z. a. Tan, *Small*, 2021, **17**, 200736.
10 C. B. Kang, M. F. Prodanov, Y. Y. Gao, K. Mallem, Z. G. Yuan, V. V. Vashchenko and A. K. Srivastava, *Adv. Mater.*, 2021, **33**, 2104685.
11 A. K. Srivastava, W. L. Zhang, J. Schneider, J. E. Halpert and A. L. Rogach, *Adv. Sci.*, 2019, **6**, 1901345.
12 J. Planelles, F. Rajadell and J. I. Climente, *J. Phys. Chem. C*, 2016, **120**, 27724–27730.
13 A. Onal, S. Sadeghi, R. Melikov, O. Karatum, G. O. Eren and S. Nizamoglu, *ACS Photonics*, 2022, **9**, 3268–3278.
14 P. Liu, S. Singh, Y. Guo, J. Wang, H. Xu, C. Silien, N. Liu and K. M. Ryan, *Sci. Rep.*, 2017, **7**, 43884.
15 A. Singh, C. Coughlan, F. Laffir and K. M. Ryan, *ACS Nano*, 2012, **6**, 6977–6983.
16 M. Zanella, R. Gomes, M. Povia, G. Cinzia, Y. Zhang, A. Riskin, M. V. Bael, Z. Hens and L. Manna, *Adv. Mater.*, 2011, **23**, 2205–2209.
17 A. Singh, R. D. Gunning, A. Sanyala and K. M. Ryan, *Chem. Commun.*, 2010, **46**, 7193–7195.
18 P. Rastogi, F. Palazon, M. Prato, F. D. Stasio and R. Krahne, *ACS Appl. Mater. Interfaces*, 2018, **10**, 5665–5672.
19 Y. Zhang, X.-M. Pham, T. Keating, N. Jia, A. Mullen, D. Laishram, M.-Y. Gao, B. Corbett, P. Liu, X. W. Sun, T. Soulimane, C. Silien, K. M. Ryan, Z. Ma and N. Liu, *ACS Appl. Mater. Interfaces*, 2024, **16**, 10459–10467.
20 Y. Zhang, N. Jia, D. Laishram, K. H. Shah, L. Lyu, M.-Y. Gao, P. Liu, X. W. Sun, T. Soulimane, Z. Ma, C. Silien, K. M. Ryan and N. Liu, *ACS Appl. Nano Mater.*, 2024, **7**, 23617–23626.

21 D. J. Shaw, *Introduction to colloid and surface chemistry*, Butterworth-Heinemann, Oxford, Boston, 4th edn, 1992.
22 H.-J. Butt and M. Kappl, *Surface and interfacial forces*, Wiley-VCH, Weinheim, 2010.
23 H. Zhang, Y. Liu, Y. Dong, A. Ashokan, A. Widmer-Cooper, J. r. Köhler and P. Mulvaney, *Langmuir*, 2024, **40**, 2783–2791.
24 K. R. Panta, C. A. Orme and B. N. Flanders, *J. Colloid Interface Sci.*, 2023, **636**, 363–377.
25 F. J. V. Santos, C. A. N. d. Castro, J. H. Dymond, N. K. Dalaouti, M. J. Assael and A. Nagashima, *J. Phys. Chem. Ref. Data*, 2006, **35**, 1–8.
26 L. Carbone, C. Nobile, M. D. Giorgi, F. D. Sala, G. Morello, P. Pompa, M. Hytch, E. Snoeck, A. Fiore, I. R. Franchini, M. Nadasan, A. F. Silvestre, L. Chiodo, S. Kudera, R. Cingolani, R. Krahne and L. Manna, *Nano Lett.*, 2007, **7**, 2942–2950.
27 H. Zhang, X. Mi, B. Kang, Y. Wu, T. Zhang, P. Liu, X. W. Sun, Z. Zhang, N. Liu and H. X. Xu, *ACS Omega*, 2023, **8**, 3762–3767.
28 W. K. Bae, L. A. Padilha, Y.-S. Park, H. McDaniel, I. Robel, J. M. Pietryga and V. I. Klimov, *ACS Nano*, 2013, **7**, 3411–3419.
29 S. Jia, S. Banerjee and I. P. Herman, *J. Phys. Chem. C*, 2008, **112**, 162–171.
30 M. A. Islam, Y. Xia, D. A. Telesca, M. L. Steigerwald and I. P. Herman, *Chem. Mater.*, 2004, **16**, 49–54.
31 L.-s. Li and A. P. Alivisatos, *Phys. Rev. Lett.*, 2003, **90**, 097402.
32 J. M. Caruge, J. E. Halpert, V. Wood, V. Bulovic and M. G. Bawendi, *Nat. Photonics*, 2008, **2**, 247.
33 V. Wood, M. J. Panzer, J. E. Halpert, J.-M. Caruge, M. G. Bawendi and V. Bulovic, *ACS Nano*, 2009, **3**, 3581–3586.
34 J. Caruge, J. E. Halpert, V. Bulovic and M. G. Bawendi, *Nano Lett.*, 2006, **6**, 2991–2994.
35 J. Y. Lee, S. Y. Kim and H. J. Yoon, *Adv. Opt. Mater.*, 2022, **10**, 2101361.
36 S. Rhee, D. Hahm, H. Seok, J. H. Chang, D. Jung, M. Park, E. Hwang, D. C. Lee, Y. Park, H. Kim and W. K. Bae, *ACS Nano*, 2021, **15**, 20332–20340.
37 X. Dai, Z. Zhang, Y. Jin, Y. Niu, H. Cao, X. Liang, L. Chen, J. Wang and X. Peng, *Nat. Photonics*, 2014, **515**, 96–99.
38 A. R. M. Alghamdi, M. Yanagida, Y. Shirai, G. G. Andersson and K. Miyano, *ACS Omega*, 2022, **7**, 12147–12157.
39 B. Ofuonye, J. Lee, M. Yan, C. Sun, J.-M. Zuo and I. Adesida, *Semicond. Sci. Technol.*, 2014, **29**, 095005.
40 C. Zou, Y. Liu, D. S. Ginger and L. Y. Lin, *ACS Nano*, 2020, **14**, 6076–6086.
41 W. K. Bae, Y.-S. Park, J. Lim, D. Lee, L. A. Padilha, H. McDaniel, I. Robel, C. Lee, J. M. Pietryga and V. I. Klimov, *Nat. Commun.*, 2013, **4**, 2661.